Modeling the ITER CS AC Losses Based on the CS Insert Analysis

(Article begins on next page)

Modeling the ITER CS AC losses based on the CS insert analysis

R. Bonifetto, *Associate Member, IEEE*, M. Bianchi, M. Breschi, *Senior Member, IEEE,* A. Brighenti, N. Martovetsky, L. Savoldi, *Member, IEEE*, and R. Zanino, *Senior Member, IEEE*

Abstract—The cable-in-conduit conductor that will be used for the manufacturing of the ITER Central Solenoid (CS) modules has undergone a long series of qualification tests: the latest was performed in 2015 at QST, Naka (Japan) on the Central Solenoid Insert (CSI) coil. In this work, the AC losses dataset collected during the CSI test campaign is interpreted using a lumped-parameter model for the coupling and hysteresis losses. The model is first benchmarked against the results of the THELMA code and then, after the implementation in the 4C thermal-hydraulic code, successfully validated against experimental data from tests performed on the CSI. With the validated AC loss model, the predictive analysis of the performance of the ITER CS is then carried out using again the 4C code, both in nominal conditions and with a reduced coolant mass flow rate in the most loaded pancake; it is shown that the minimum temperature margin required by the design is always satisfied, for both virgin (1 K) and cycled (1.5 K) conductor.

Index Terms—AC loss modeling, cable in conduit conductors, fusion magnets, ITER CS, thermal-hydraulics.

I. INTRODUCTION

THE ITER Central Solenoid (CS) modules are being procured by the US-ITER project office [1]. All the cable-in-conduit conductors (CICCs) used to wind the 6 modules (plus one spare) of the CS have been qualified by means of suitable tests carried out on several samples, including short samples [2], tested in the SULTAN facility in Villigen, Switzerland, and a full-scale long conductor [3], tested in the bore of the ITER CS Model Coil (CSMC) [4] in Naka, Japan. After fabrication, the modules are going to be cold-tested in a new facility at General Atomics (GA) in San Diego, California [5], [6]. The aim of these tests is to verify the performance of the CS modules in ITER-relevant operating conditions [6]. With respect to the conductor tests, the module cold-tests are also expected to provide data on the effects of thermal coupling inside the winding pack, where the conductors are wound in hexa- and quad-pancakes, with thermal contact between different turns and pancakes.

Since the CS is a pulsed coil, the most relevant internal heat source during operation in the tokamak is due to AC losses induced by the current variation. Several relevant AC loss data were collected during the last CS Insert (CSI) coil test campaign in 2015 [3], in the framework of the qualification tests performed on the ITER CS conductor: here we interpret the CSI experimental dataset using an analytical model for the hysteresis and coupling losses in the cable. The model is first benchmarked against the numerical results [7] of the electro-magnetic module of the THELMA code [8], giving very good agreement. Afterwards, it is implemented in the state-of-the-art thermal-hydraulic (TH) 4C code [9], and validated against data from the CSI test campaign, by means of a comparison between the computed and measured TH variables at the CSI boundaries and the temperatures at several axial locations along the conductor, in order to confirm the accuracy of the analytical AC loss model. Finally the validated model, which allows the reliable calculation of the evolution and distribution of the power generated by AC losses (mostly coupling and hysteresis losses) and deposited in the conductor, is applied to the entire ITER CS. Since the 4C code can accurately describe the heat diffusion between neighboring CICC turns and pancakes/layers, which is fully relevant in the case of the ITER CS [10], the effects of the AC losses induced by different current ramps during the standard 15 MA ITER plasma scenario [11] is analyzed predictively in the entire winding pack of the CS.

II. EXPERIMENTAL SETUP AND DATA

The CSI, manufactured with the very same conductor of the ITER CS, is a ~43 m long conductor wound in 9 turns separated by an epoxy spacer and supported by two stainless steel (SS) spacers which, together with the flanges, constitute the coil support structure, see Fig. 1. The CSI was tested in ITER-relevant operating conditions in 2015 at QST, Naka (Japan), inside the bore of the ITER CSMC [4]. Details of the test campaign, CSI
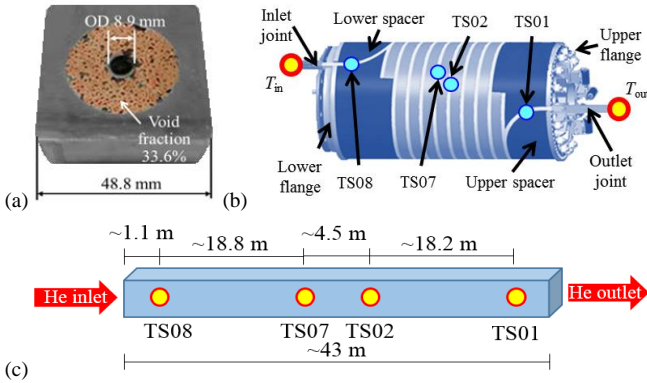
Fig. 1. (a) Cross section of the CSI conductor. (b) Sketch of the CSI with the relevant sensors for the AC loss tests highlighted. (c) Location of the temperature sensors along the CSI.

conductor geometry and experimental setup can be found in [3], [12] and [7], respectively. The qualification of the AC losses in the conductor [13], [14], and the analysis of their evolution with electromagnetic cycling [15], were some of the main objectives of the test campaign.

AC losses in the CSI were measured during exponential dumps of the current in the CSMC (i.e. of the external magnetic field in which the CSI was placed), with a characteristic time constant $T_d \sim 20$ s. As the two coils have different dump time constants, to avoid the mix of different power deposition timescales only shots with no current in the CSI have been selected.

For the analysis and assessment of the conductor AC performance, a set of experimental shots has been identified (see Table I), including tests both at the beginning and at the end of electromagnetic cycles (BoC and EoC, respectively).

III. ANALYTICAL MODEL

Coupling losses per unit length (P_{coup}) in the cable [16] can be modeled as:

$$P_{coup}(t) = \frac{n\tau}{\mu_0} \cdot \dot{B_i}^2(t) \cdot A_{st} \qquad (1)$$

where $n\tau$ [s] is the coupling time constant of the cable, μ_0 [H/m] the magnetic permeability of the vacuum, $\dot{B_i}$ [T/s] the derivative of cable internal field and A_{st} [m²] the total cross section of the composite strands.

The internal magnetic field B_i depends on the external magnetic field B_e according to [17], [18]:

TABLE I
PARAMETERS FOR SELECTED AC LOSS TESTS, WITH NO CURRENT IN THE CSI ($I_{0,CSI} = 0$).

Shot #	$I_{0,CSMC}$ [kA]	Cycle #
36-1	23	BoC
37-1	36.8	BoC
40-1	46	BoC
80-4	23	1000
97-4	23	5000
129-1	23	10000
164-4	23	EoC$^\$$
188-4	46	EoC$^\&$

$^\$$ Tests performed at EoC, namely after 16000 EM cycles.
$^\&$ Tests performed at EoC and after quench (Q) tests.

$$B_i(t) = B_e(t) - \dot{B_i}(t)\frac{n\tau}{2} \qquad (2)$$

which allows to determine the specific formulation of P_{coup}.

A. Coupling losses during exponential magnetic field dump

The external field B_e, provided in this experiment by the CSMC, decays exponentially from the initial value B_0 according to the following expression

$$B_e(t) = B_0 e^{-\frac{t}{T_d}} \qquad (3)$$

where T_d is the magnetic field dump time constant.

Solving (2) for $B_i(t)$ and substituting it in (1), yields the following expression for the coupling losses:

$$P_{coup}(t) = \frac{n\tau}{\mu_0} \left(\frac{B_0}{T_d - \frac{n\tau}{2}} \left(e^{-\frac{t}{\frac{n\tau}{2}}} - e^{-\frac{t}{T_d}} \right) \right)^2 A_{st} \qquad (4)$$

which is valid only for an exponential decrease of the field B_e.

B. Coupling losses during linear magnetic field ramp

If the magnetic field (B_e) varies according to a (descending) linear ramp, the external magnetic field can be written as

$$B_e(t) = -\frac{B_0}{T_r}t + B_0 \qquad (5)$$

where T_r [s] is the duration of the ramp.

Inserting (5) in (2), solving (2) to determine $B_i(t)$, and substituting the result in (1), gives the expression of the time dependent linear power density:

$$P_{coup}(t) = \frac{n\tau}{\mu_0} \left(\frac{B_0}{T_r} \left(e^{-\frac{t}{\frac{n\tau}{2}}} - 1 \right) \right)^2 A_{st} \qquad (6)$$

which is valid only for a linear evolution of B_e, due to (5).

C. Hysteresis losses

The hysteresis losses in the cable per unit length (P_{hyst}) are computed as [19]:

$$P_{hyst} = \frac{2 \cdot J_c \cdot d_{eff} \cdot |\dot{B_e}| \cdot A_{nonCu}}{3\pi} \qquad (7)$$

where J_C is the local current density at (x,t), $\dot{B_e}$ is the magnetic field derivative, A_{nonCu} is the cross section of non-Cu material in the composite strands and $d_{eff} = 19$ µm is the effective diameter of the superconducting filaments. The value of the latter was determined by calorimetry in [20], but in view of the very small temperature increase during hysteresis measurements it was considered subject to some uncertainty. For this reason, starting from that reference value, a calibration has been performed here, resulting in a $d_{eff} = 29$ µm from a best fit of the temperature evolution during slow linear ramps of the magnetic field (when $P_{hyst} \gg P_{coup}$).

IV. CALORIMETRY FOR THE ESTIMATION OF $n\tau$

The coupling time constant $n\tau$ in the lumped-parameter model described above can be obtained from the total energy E deposited in the CSI during the AC loss tests. The energy deposited in the cable region included between the TS07 and TS02 temperature sensors, see Fig. 1c, is computed as in [7]:

$$E = \int_{t_{dump}}^{\infty} (h_2(\bar{p}, T_2) - h_7(\bar{p}, T_7)) \times \dot{m}_{ave} dt \qquad (8)$$

where t_{dump} is the dump time, h the specific enthalpy evaluated locally for the two sensors and $\bar{p}$ and $\dot{m}_{ave}$ are the pressure and mass flow rate computed as average between inlet and outlet measurements.

The energy deposited in the CSI by coupling losses is obtained removing from the total energy the estimated contribution from the hysteresis losses E_{hyst}, computed by time integration of (7), i.e.

$$E_{coup,CSI} = E - E_{hyst} \qquad (9)$$

The integration of P_{coup} in (4) over time and space, with $t \in [t_{dump}, \infty]$ and $x \in [x_{TS07}, x_{TS02}]$, corresponds to $E_{\text{coup,CSI}}$: by dividing it for $A_{st} \cdot (x_{TS02} - x_{TS07})$ we obtain the energy per unit volume of composite strands, $q_{\text{coup,CSI}}$. Therefore, solving for $n\tau$, it is possible to deduce its value from experimental data:

$$n\tau = \frac{2q_{coup,CSI}T_d\mu_0}{\overline{B_e^2} - q_{coup,CSI}\mu_0} \qquad (10)$$

where $\overline{B_e^2}$ is the square of the integral average (external) magnetic field in the region within the TS07 and TS02 temperature sensors.

The calorimetry and the estimated $n\tau$ values are reported in Table II. The variation of $n\tau$ with electro-magnetic cycling is reported in Fig. 2, showing that in less than 1000 cycles it reduces by a factor ~ 3 (from ~ 600 ms to ~ 200 ms). Note that the $n\tau$ value at EoC is still larger than prescribed (75 ms [21]).

V. THELMA ELECTRICAL MODEL

The electrical module of the THELMA code [8] is a state-of-the-art model for the computation of current distribution and AC losses in multistrand superconducting cables for fusion [22], and accelerator magnets [23], [24].

The model represents the conductor through a distributed parameter non-linear circuit. The cable is subdivided into a set of electrical elements, which can either correspond to individual
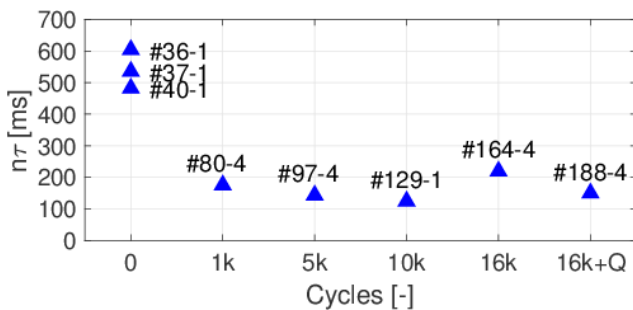
TABLE II
MAIN RESULTS FOR SELECTED TESTS

Shot #	T_d [s]	$I_{0,CSMC}$ [kA]	B_0 [T]	$E_{coup,CSI}$ [kJ]	$n\tau$ [ms]
36-1	19.1	23.1	6.06	0.69	590
37-1	19.2	36.8	9.68	1.58	530
40-1	18.3	46.1	12.1	2.17	470
80-4	18.5	23	6.04	0.20	175
97-4	18	23	6.04	0.16	143
129-1	18.5	22.9	6.02	0.14	124
164-4	18.9	23.0	6.04	0.25	220
188-4	19.6	45.9	12.1	0.69	149

wires or to strand bundles. The strands/sub-cables interact with each other by means of electrical conductances and mutual inductances. The interaction of the electrical elements with external coils is also considered through mutual inductive coupling.

In the THELMA model of the CSI, the conductor is represented at the level of the 24 sub-cables of the last but one cabling stage, each composed of 36 strands. The geometry of the CSI conductor as represented in the THELMA model is shown in Fig. 3. The inductive coupling of the CSI sub-cables with the CSMC coil allows computing directly the electromotive forces induced in the loops formed by the sub-cables during the dumps of the CSMC current. The resulting current and coupling loss distributions and evolutions are then determined.

VI. BENCHMARK AGAINST THE THELMA RESULTS

While the analytical model presented in Sections III-IV has been calibrated just using global information deriving from the CSI experimental campaign, (4) and (6) are suited also to compute the local power deposition along the cable, which is not directly measurable. The THELMA electro-magnetic model, described in Section V, has been already successfully applied in [7] to the detailed evaluation of the local power deposition in the CSI. Those results are used as reference for the benchmark of the power profile computed by the analytical model described here. It uses in input the 1D (external) magnetic field distribution along the CSI axis before the CSMC exponential current dump (the one for Shot #36-1, used as reference for the benchmark, is reported in Fig. 4a). That distribution is scaled proportionally to the CSMC current (I_{CSMC}) evolution
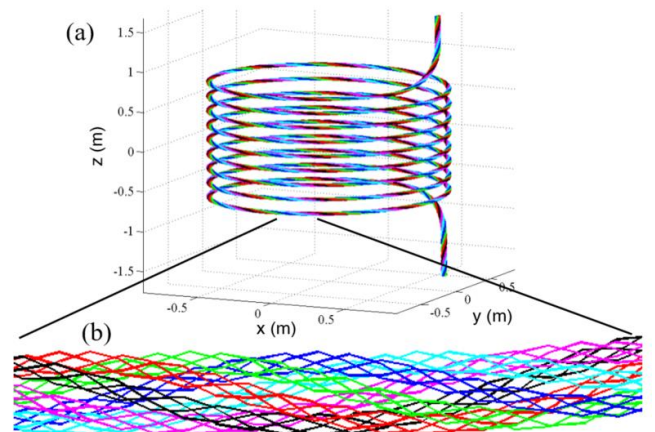

Fig. 3. (a) Geometry of the CSI represented with the THELMA code through 24 sub-cables. (b) Detailed geometry of the sub-cables composing the CS conductor.

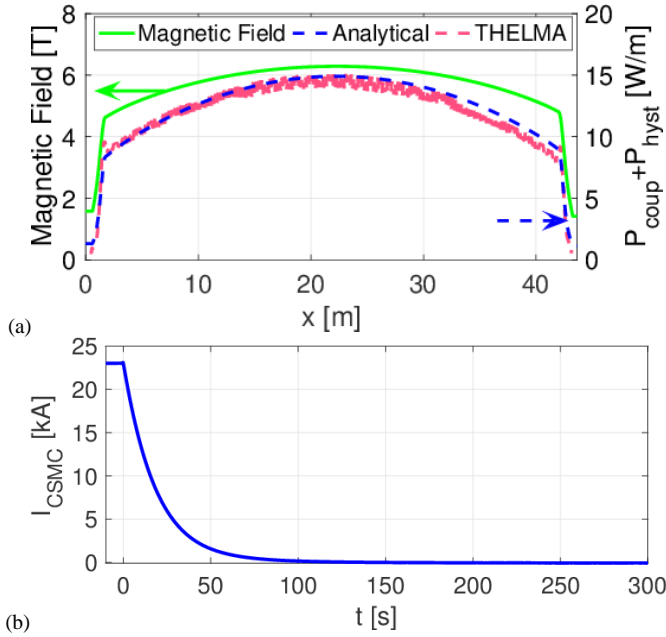Fig. 2. Variation of the $n\tau$ with the number of cycles in the CSI.

(a)

(b)

Fig. 4. For Shot #36-1, (a) magnetic field (left axis) distribution along the CSI conductor axis before the CSMC current dump (solid green), total (coupling and hysteresis) linear power density profile along the CSI (right axis) at $t = 1$ s after the dump start according to the analytical model (dashed blue) and THELMA (dashed pink) results. (b) Current evolution in CSMC during Shot #36-1.

($T_d \sim 19$ s), shown in Fig. 4b. The resulting linear power deposition due to AC losses computed by the analytical model is compared with that of THELMA in Fig. 4a. It is shown that both approaches are equivalent within 10% and that the power profile reflects the magnetic field distribution; the differences are due to the use of a model (the analytical one) developed for a uniform magnetic field (which is not the case close to the CSI boundaries), perpendicular to the cable.

The power evolution computed by the detailed THELMA model is nicely approximated by the analytical model, see Fig. 5: the differences between the two approaches can be attributed to the approximation of the coupling losses with a single time constant in the analytical model.

Despite the small local difference in the power evolution, the total energy deposited is obviously the same for both models and corresponds to the experimental value of $E_{coup,CSI}$, used for the $n\tau$ estimation.
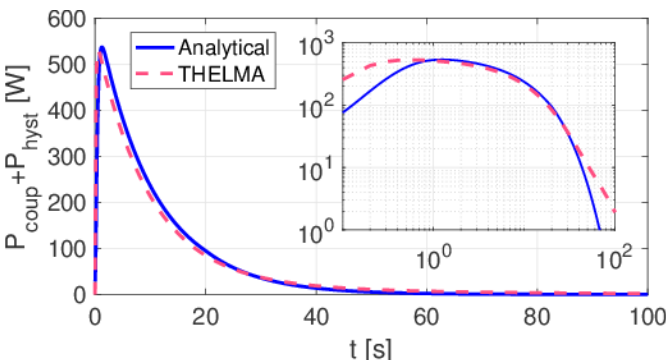
VII. 4C CODE THERMAL-HYDRAULIC MODEL

The 4C code [9] model of the CSI coil is the same already used to perform the thermal-hydraulic simulations in [7]. Two Euler-like 1D sets of equations allow computing the velocity, pressure and temperature of the supercritical helium (SHe), used as a coolant, in the central hole and in the (bundle) annular region of the CICC, while transient 1D heat conduction equations are solved to evaluate the temperature of the strands and of the jacket, respectively. Coupling terms model the heat transfer between the solids and the fluid, and between the two SHe regions. Selected 2D cross sections of the supporting structure, thermally coupled with the conductor jacket, are also included, accounting for the eddy current losses during the current dump [25] (as done in [7]) and for the heat sink provided by the structures cooling channel. More details about the model can be found in [26].

After the successful benchmark of the analytical model vs. THELMA, the analytical model has been implemented in 4C, taking as input the $n\tau$ value derived from CSI data analyses. A subset of the selected shots has been simulated using the $n\tau$ in Table II, to validate the 4C code implementing the new analytical model for the AC loss calculation.

The scaling parameters used for the evaluation of the critical current density are the same reported in [27].

VIII. AC LOSSES ASSESSMENT

The computed temperature evolutions at the TS07 and TS02 sensor locations have been compared with experimental data of shot #36-1, see Fig. 6. The mismatch (average relative error) between the computed and the experimental temperature evolutions is $< 11\%$. Concerning the $\dot{m}$, the simulations reproduce the phenomenology of the measured data within the experimental error bar, see Fig. 7, while the decrease of inlet $\dot{m}$ is overestimated by the computed results; this is possibly correlated with some issues on the dynamic response of the mass flow sensors, as already highlighted in [7].

The analytical model is used to confirm the validity of the lumped-parameter approach simulating also other shots, as e.g. #40-1. The results are reported in Fig. 8. Note that the agreement between computed and measured temperature evolution at sensors TS08 and TS01, far from the central zone where the magnetic field is ~uniform and perpendicular to the cable itself,

Fig. 5. Total power evolution in the CSI for Shot #36-1 according to the analytical model (solid blue) and THELMA (dashed pink) results.
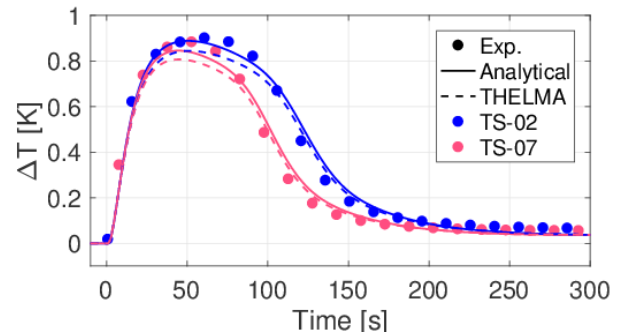

Fig. 6. Temperature increase evolution at TS07 (pink) and TS02 (blue) sensors for Shot #36-1: experimental (solid with circles) and computed results using 4C with analytical model (solid) and power input from THELMA (dashed).
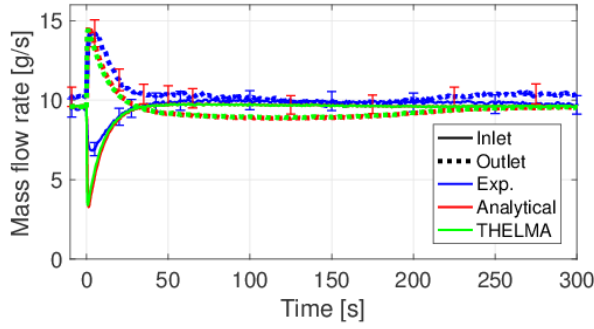
Fig. 7. $\dot{m}$ evolution at inlet (solid) and outlet (thick dotted) for Shot #36-1: experimental (blue) and computed results using the analytical model (red) and THELMA (green).

is only qualitative. This is due to the fact that the analytical model was developed assuming a uniform magnetic field. This is not true near the boundaries of the coil, where large B gradients arise, while it is still applicable to each turn of the ITER CS, featuring a ~ constant magnetic field. The average relative error, evaluated on TS07, TS02 and TS01, is again < 11%, while on TS08 it is much larger, in view of the large B gradient on that zone. Indeed, an overestimation of the temperature increase is computed also at TS01, suffering of the same B gradient; however, it is less evident due to the higher temperature increase measured by that sensor, which is located close to the CSI outlet and therefore measures the increase due the heat deposition in the whole CSI.

IX. PROJECTED OPERATION OF THE ITER CS

Since the analytical model, when implemented in 4C, is very fast and gives very encouraging results when compared to the experimental data, the model in (6) (suitable for linear ramps of the magnetic field), together with the hysteresis loss model in (7) will now be used to assess the performance of the entire ITER CS during operation.

A. Model and simulation setup

The 4C model of the ITER CS adopted here is the same used in [28], see Fig. 9: the CS is constituted by 6 different modules and each one is made of seven Nb₃Sn conductors wound in 6
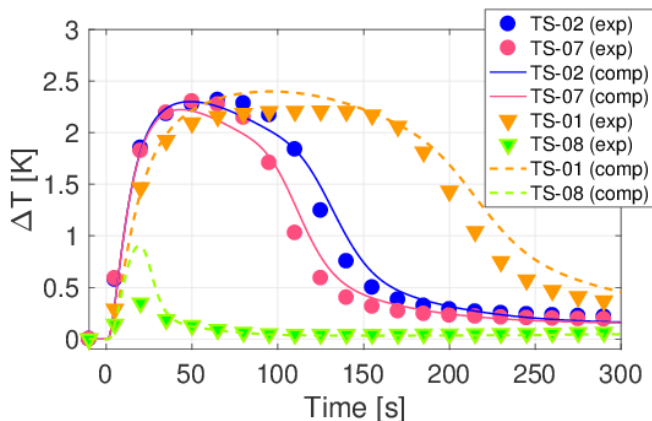

Fig. 8. Temperature increase evolution at selected sensor locations for Shot #40-1 computed by 4C using the analytical model for the AC losses.
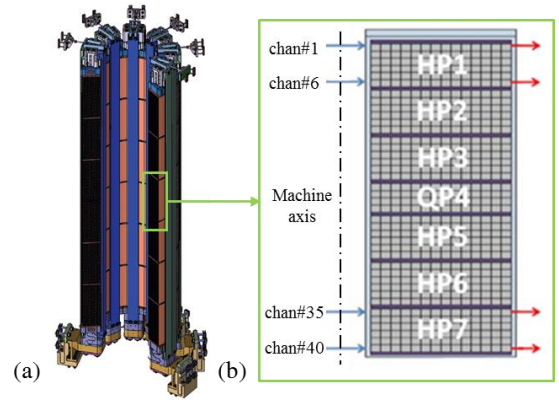

Fig. 9. (a) Representation of the full ITER CS (reproduced from [29]) and (b) detail of the cross section of one of the modules. The location of the SHe inlets and outlets is also shown by the arrows in (b).

hexa-pancakes (HP) and 1 quad-pancake (QP) for a total of 240 pancakes in the whole coil.

The modules are cooled in parallel by forced flow SHe, releasing the heat load to a liquid helium (LHe) bath through a heat exchanger, see Fig. 10.

Each pancake is cooled in parallel to the others; the SHe is supplied from the CS bore, while the outlets are located at the outer radius of the coil, see Fig. 9b.

All the 240 parallel channels are accounted for in the 4C model, each of them ideally with the same hydraulic length. Each channel has its own He inlet located at the inner side of the module. Counter-current He flow in neighbouring channels and the thermal coupling between neighboring CICC turns and pancakes inside each module are taken into account. The scheme of the primary cooling circuit model is reported in Fig. 10: the pump operating point provides a total $\dot{m}$ ~2 kg/s with a pressure head of ~0.084 MPa (coil inlet pressure ~ 4 bar). The coil inlet temperature is set to the nominal value of 4.3 K, coincident with the LHe bath temperature. Nuclear and static (radiative and conductive) heat loads are neglected.

The strain is computed locally as a function of $I \times B(x,t)$. The function adopted here is that described in [27], obtained as a projection of the CSI one to ITER CS operation.

Simulations were performed for the ITER standard 15 MA current scenario for each module, see Fig. 11 [11].

The coil performance is assessed considering the $n\tau$ values computed for the CSI at BoC (i.e. for the *virgin* conductor) and at EoC (i.e. for the *cycled* conductor), corresponding to those
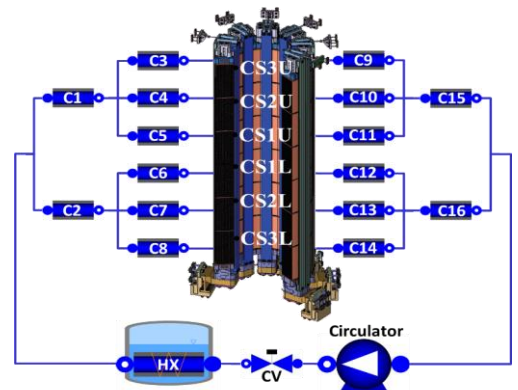

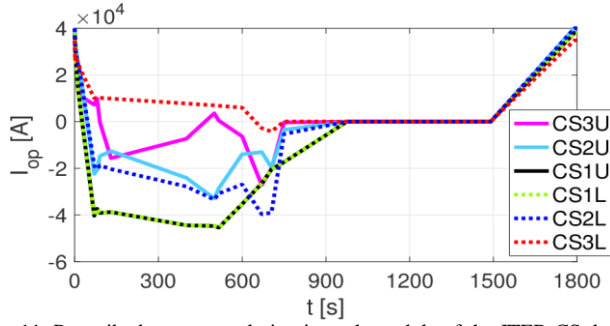Fig. 10. Model of ITER CS coil cooling circuit adopted in the simulations.

Fig. 11. Prescribed current evolution in each module of the ITER CS during the standard 15 MA plasma pulse.

determined for Shots #36-1 (590 ms) and #164-4 (220 ms), as they show conservatively the highest $n\tau$ values for virgin and cycled conductor, respectively, see Fig. 2.

B. Results

The large power deposition in the first phases of the pulse causes a strong pressurization, inducing backflow at the inlet of the modules, see Fig. 12. However, the two central modules (i.e. CS1U/1L), where the power deposited is smaller, experience a lower pressurization, so that the mass flow rate expelled from the backflow in the other modules (connected in tight hydraulic parallel) contributes to increase the inlet mass flow rate in the two central modules.

During the nominal operation of the CS, the absolute minimum temperature margin (ΔT_{marg}^{min}) in the coil, see Fig. 13, rapidly decreases during the breakdown because B and its derivative have large values. Then, ΔT_{marg}^{min} starts increasing again for the combination of the decreased heat deposition, proportional to $(\dot{B})^2$, and B. However, at ~ 70 s the ΔT_{marg}^{min} decreases again because B is increasing, and from ~ 100 s to 900 s the margin increases, because of the small power deposited (small $\dot{B}$). Then during the dwell (from 900 s to 1500 s), the margin is almost constant because the coil is not charged, while from 1500 s to the end of the pulse, during the coil recharge, the margin decreases again.

The ITER CS satisfies the minimum requirement of 1 K with virgin conductor and 1.5 K with cycled conductor [30]. For a virgin conductor, the minimum value is reached in module
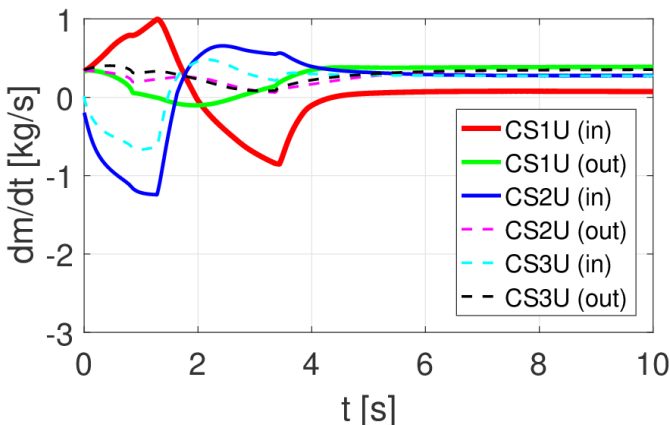

Fig. 12. Evolution of inlet/outlet $\dot{m}$ for the upper CS modules at the beginning of the nominal pulse for a cycled conductor.
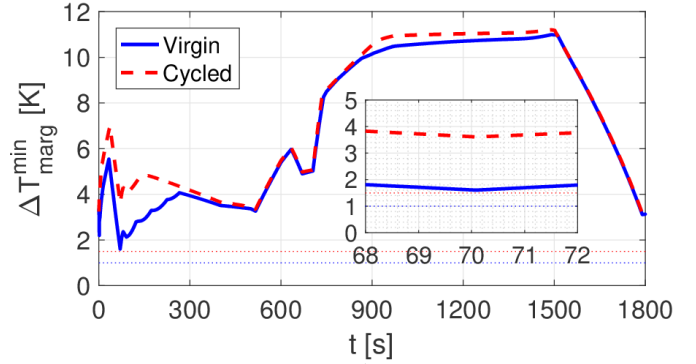

Fig. 13. Evolution of the absolute ΔT_{marg}^{min} in the CS with the $n\tau$ evaluated for the virgin (solid blue) and cycled (dashed red) conductor. The minimum requirements are also reported as horizontal dotted lines.

CS1L before the plasma start at ~70 s (when lot of heat has been accumulated during previous current ramps), while for a cycled conductor, the minimum value is reached in module CS2U in the first instants of the discharge, when the magnetic field and its derivative have their maximum values, see Fig. 14.

In addition, a parametric study on the $\dot{m}$ in the most critical (virgin) conductor has been performed for the most critical pancake: the nominal $\dot{m}$ ~ 8.3 g/s has been reduced of ~ 25%, to take into account the uncertainty on the friction factor and on the effective hydraulic length of the cooling channels, which may differ from the ideal value adopted in the model. The reduction of the $\dot{m}$ for a virgin conductor in channel #9 shows that the ΔT_{marg}^{min} is reduced of ~0.3 K, see Fig. 15, so that if the 10% of uncertainty from the analysis of the CSI AC losses is accounted for, it can fall below the acceptance limit (1 K). In adjacent pancakes the ΔT_{marg}^{min} erosion is few mK, as they take care of part of the heat deposited in the conductor with reduced $\dot{m}$.

X. CONCLUSIONS

A lumped-parameter analytical model for AC loss calculation in the ITER CS conductor has been derived and successfully benchmarked against a more detailed computational model, proving to be capable to compute almost identical AC loss power deposition. It was also successfully validated based on the CSI test results.

According to the results obtained with the analytical model, the $n\tau$ value of the CS conductor extracted from the experimental data is estimated to reduce from ~ 590 ms to ~ 220 ms after EM cycling.
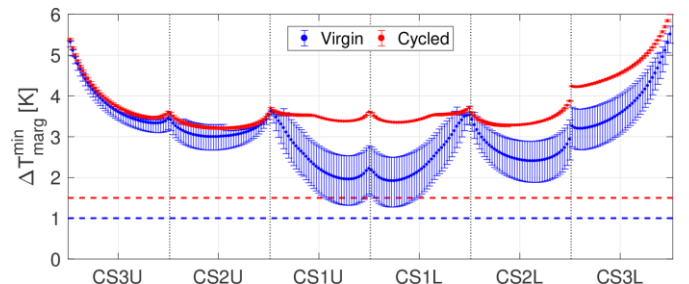

Fig. 14. ΔT_{marg}^{min} with estimated error bar in each conductor of the CS with the coupling time constant evaluated for the virgin (blue) and cycled (red) conductor.
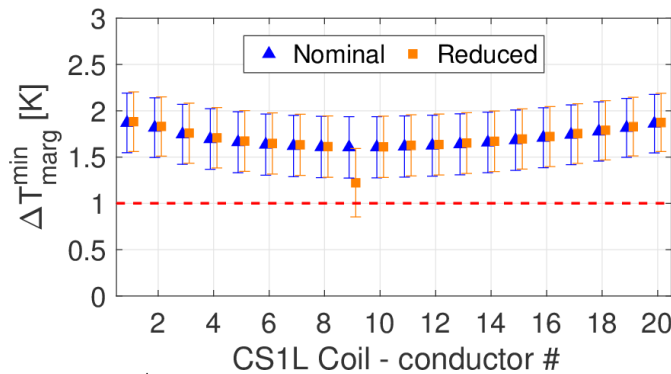
This article has been accepted for publication in a future issue of this journal, but has not been fully edited. Content may change prior to final publication. Citation information: DOI 10.1109/TASC.2019.2903626, IEEE Transactions on Applied Superconductivity

7

Fig. 15. $\Delta T_{\mathrm{marg}}^{\min}$ in CS1L module with nominal (blue triangles) and reduced (orange squares) $\dot{m}$ in most critical channel (#9) for a virgin conductor. The horizontal red line shows the minimum temperature margin requirement for a virgin conductor.

Despite even the latter value is still greater than ITER specifications (75 ms), when these $n\tau$ values are applied to the analysis of the standard 15 MA plasma pulse in ITER, both for a virgin and cycled conductor, all CS conductors satisfy the requirement on $\Delta T_{\mathrm{marg}}^{\min}$.

In the case of reduction of the mass flow in a pancake by ~ 25%, the temperature margin is eroded by ~ 0.3 K. In this scenario, the requirement can be not satisfied by less than 0.2 K.

REFERENCES

[1] P. Libeyre, C. Cormany, N. Dolgetta, E. Gaxiola, C. Jong, C. Lyraud, N. Mitchell, J. Y. Journeaux, R. Pearce, D. Evans, S. Sgobba, S. Langeslag, I. Aviles, W. Reiersen, N. Martovetsky, D. Everitt, D. Hatfield, T. Chae, D. Hughes, T. Reagan, S. Litherland, K. Freudenberg, J. Smith, D. M. McRae, and R. P. Walsh, "Manufacture of the ITER Central Solenoid Components," *IEEE Trans. Appl. Supercond.*, vol. 28, no. 3, Apr. 2018, Art. no. 4200805.

[2] T. Hemmi, Y. Nunoya, Y. Nabara, M. Yoshikawa, K. Matsui, H. Kajitani, K. Hamada, T. Isono, Y. Takahashi, N. Koizumi, H. Nakajima, B. Stepanov, and P. Bruzzone, "Test results and investigation of Tcs degradation in Japanese ITER CS conductor samples," *IEEE Trans. Appl. Supercond.*, vol. 22, no. 3, Jun. 2012, Art. no. 4803305.

[3] N. Martovetsky, T. Isono, D. Bessette, Y. Takahashi, Y. Nunoya, Y. Nabara, H. Ozeki, K. Kawano, T. Saito, T. Suwa, K. Okuno, A. Devred, F. Gauthier, N. Mitchell, R. Zanino, L. Savoldi, R. Bonifetto, M. Breschi, D. Ciazynski, W. Reiersen, A. Smirnov, A. Khodak, P. Bruzzone, I. Rodin, V. Tronza, A. Torre, S. Nicollet, L. Zani, A. Louzguiti, and J. L. Duchateau, "ITER central solenoid insert test results", *IEEE Trans. Appl. Supercond.*, vol. 26, no. 4, Jun. 2016, Art. no. 4200605.

[4] H. Tsuji, K. Okuno, R. Thome, E. Salpietro, S. Egorov, N. Martovetsky, M. Ricci, R. Zanino, G. Zahn, A. Martinez, G. Vecsey, K. Arai, T. Ishigooka, T. Kato, T. Ando, Y. Takahashi, H. Nakajima, T. Hiyama, M. Sugimoto, N. Hosogane, M. Matsukawa, Y. Miura, T. Terakado, J. Okano, K. Shimada, M. Yamashita, T. Isono, N. Koizumi, K. Kawano, M. Oshikiri, Y. Nunoya, K. Matsui, Y. Tsuchiya, G. Nishijima, H. Kubo, T. Shimba, E. Hara, K. Imahashi, Y. Uno, T. Ohuchi, K. Ohtsu, J. Okayama, T. Kawasaki, M. Kawabe, S. Seki, K. Takano, Y. Takaya, F. Tajiri, F. Tsutsumi, T. Nakamura, H. Hanawa, H. Wakabayashi, T. Shimizu, K. Kuramochi, T. Omine, T. Tamiya, J. Harada, K. Nishii, M. Huguet, N. Mitchell, D. Bessette, J. Minervini, R. Vieira, P. Michael, M. Takayasu, G. Bevilacqua, R.K. Maix, R. Manahan, R. J. Jayakumar, L. Savoldi, W. Herz, and A. Ninomiya, "Progress of the ITER Central Solenoid Model Coil program," *Nucl. Fusion*, vol. 41, 2001, pp. 645-651.

[5] J. Spitzer, A. Stephens, K. Schaubel, J. Smith, N. Norausky, K Khumthong, and A. Gattuso, "ITER Central Solenoid Module fabrication program," *Proceedings of 2015 IEEE 26th Symposium on Fusion Engineering* (SOFE), 2015.

[6] K. Schaubel, A. Langhorn, S. Lloyd, Z. Piec, E. Salazar, and J. Smith, "The ITER Central Solenoid Module final test facility," *Fus. Eng. Des.*, vol. 124, 2017, pp. 59-63.

[7] M. Breschi, M. Bianchi, R. Bonifetto, S. Carli, A. Devred, N. Martovetsky, P. L. Ribani, L. Savoldi, I. Takaaki, and R. Zanino, "Analysis of AC losses in the ITER Central Solenoid Insert (CSI) Coil," *IEEE Trans. Appl. Supercond.*, vol. 27, no. 4, Jun. 2017, Art. no. 4200605.

[8] M. Ciotti, A. Nijhuis, P. L. Ribani, L. Savoldi Richard, and R. Zanino, "Thelma code electromagnetic model of ITER superconducting cables and application to the ENEA stability experiment," *Supercond. Sci. Technol.*, vol. 19, no. 10, 2006, pp. 987-997.

[9] L. Savoldi Richard, F. Casella, B. Fiori, and R. Zanino, "The 4C code for the cryogenic circuit conductor and coil modeling in ITER," *Cryogenics*, vol. 50, no. 3, Mar. 2010, pp. 167-176.

[10] R. Zanino, N. Mitchell, and L. Savoldi Richard, "Analysis and interpretation of the full set (2000–2002) of T_{CS} tests in conductor 1A of the ITER Central Solenoid Model Coil," *Cryogenics*, vol. 43, 2003, pp. 179-197.

[11] A. Devred, D. Bessette, P. Bruzzone, K. Hamada, T. Isono, N. Martovetsky, N. Mitchell, Y. Nunoya, K. Okuno, I. Pong, W. Reiersen, C. M. Rey, B. Stepanov, Y. Takahashi, and A. Vostner, "Status of Conductor Qualification for the ITER Central Solenoid," *IEEE Trans. Appl. Supercond.*, vol. 23, no. 3, Jun. 2013, Art. no. 6001208.

[12] T. Isono, K. Kawano, H. Ozeki, H. Kajitani, N. Koizumi, K. Okuno, T. Minato, H. Nishimiya, Y. Watabe, H. Sakamoto, T. Sasaki, A. Smirnov, and N. Martovetsky, "Fabrication of an Insert to Measure Performance of ITER CS Conductor," *IEEE Trans. Appl. Supercond.*, vol. 25, no. 3, Jun. 2015, Art. no. 4201004.

[13] A. Nijhuis, E. P. A. Van Lanen, and G. Rolando, "Optimization of ITER Nb3Sn CICCs for coupling loss, transverse electromagnetic load and axial thermal contraction," *Supercond. Sci. Technol.*, vol. 25, no. 1, Dec. 2011, Art. no. 015007.

[14] G. Rolando, A. Devred, and A. Nijhuis, "Minimizing coupling loss by selection of twist pitch lengths in multi-stage cable-in-conduit conductors," *Supercond. Sci. Technol.*, vol. 27, 2014, Art. no. 015006.

[15] D. Bessette, "Design of a Nb3Sn Cable-in-Conduit Conductor to Withstand the 60 000 Electromagnetic Cycles of the ITER Central Solenoid," *IEEE Trans. Appl. Supercond.*, vol. 24, no. 3, Jun. 2014, Art. no. 4200505.

[16] M. N.Wilson, SuperconductingMagnets. Oxford, U.K.: Clarendon, 1983.

[17] B. Turck, and L. Zani, "A macroscopic model for coupling current losses in cables made of multistages of superconducting strands and its experimental validation," *Cryogenics*, vol. 50, no. 8, 2010, pp. 443-449.

[18] A. Louzguiti, L. Zani, D. Ciazynski, B. Turck, and F. Topin, "Development of an analytical-oriented extensive model for AC coupling losses in multilayer superconducting composites," *IEEE Trans. Appl. Supercond.*, vol. 26, no. 3, Apr. 2016, Art. no. 4700905.

[19] P. Fabbricatore, "Dynamic effects on superconducting dipoles used for an ion beam cancer therapy gantry," presented at the 2nd Beam Dynamics Meets Magnets Workshp, Bad Zurzach (Switzerland), December 1-4, 2014.

[20] D. Bessette, presentation at CS Insert test results Workshop, Naka, Japan, Oct. 2015.

[21] ITER Design Description Document (DDD) 11 Magnets, 7 Conductors, 2009.

[22] M. Breschi, M. Bianchi, A. C. Ricchiuto, P. L. Ribani, and A. Devred, "Analysis of AC Losses in a CS Conductor Sample for the ITER Project", *IEEE Trans. Appl. Supercond.*, vol. 28, n. 3, 2018, Art. no. 5900205.

[23] M. Breschi, A. Macchiagodena, P. L. Ribani, F. Bellina, F. Stacchi, S. Izquierdo Bermudez, and H. Bajas, "Experimental and Numerical Investigation on Losses in Electrodynamic Transients in a Nb3Sn Prototype Racetrack Coil," *IEEE Trans. Appl. Supercond.*, vol. 28, n. 3, 2018, Art. no. 4000605.

[24] M. Breschi, L. Cavallucci, P. L. Ribani, C. Calzolaio, and S. Sanfilippo, "Analysis of losses in superconducting magnets based on the Nb3Sn Rutherford cable configuration for future gantries", *Supercond. Sci. Technol.*, vol. 31, 2018, Art. no. 015005.

[25] M. Coatanea-Gouachet, "CSI spacers—Heat generation during CSMC discharge," ITER IDM document RENCRN v1.0, 06 June 2015.

[26] R. Bonifetto, A. Brighenti, T. Isono, N. Martovetsky, K. Kawano, L. Savoldi, and R. Zanino, "Analysis of the cooldown of the ITER central solenoid model coil and insert coil," *Supercond. Sci. Technol.*, vol. 30, 2017, Art. no. 015015.

[27] N. Martovetsky, T. Isono, D. Bessette, A. Devred, Y. Nabara, R. Zanino, L. Savoldi, R. Bonifetto, P. Bruzzone, M. Breschi, and L. Zani, "Characterization of the ITER CS conductor and projection to the ITER CS performance," *Fus. Eng. Des.*, vol. 124, 2017, pp. 1-5.

[28] L. Savoldi Richard, R. Bonifetto, S. Carli, A. Froio, A. Foussat, and R. Zanino, "Artificial Neural Network (ANN) modeling of the pulsed heat

This article has been accepted for publication in a future issue of this journal, but has not been fully edited. Content may change prior to final publication. Citation information: DOI 10.1109/TASC.2019.2903626, IEEE Transactions on Applied Superconductivity

8

load during ITER CS magnet operation," *Cryogenics*, vol. 63, Sep.-Oct. 2014, pp. 231-240.

[29] P. Libeyre, C. Cormany, N. Dolgetta, E. Gaxiola, C. Jong, C. Lyraud, W. Reiersen, D. Everitt, N. Martovetsky, P. Rosenbald, M. Cole, K. Freuden- berg, S. Liu, J. Smith, J. Wei, L. Wang, X. Yu, X. Dong, J. Xin, C. Li, W. Zheng, and C. Fang, "Status of design and manufacturing of the ITER Central Solenoid and Correction Coils," *Proceedings of 2015 IEEE 26th Symposium on Fusion Engineering* (SOFE), 2015.

[30] G. Rolando, A. Devred, and A. Nijhuis, "Temperature and current margin of ITER central solenoid conductor designs during a 15 MA plasma sce- nario," *Supercond. Sci. Technol.*, vol. 27, no. 2, Dec. 2014, Art. no. 025010.